Supporting Information

Oriented Construction of Efficient Intrinsic Proton Transport in MOF-808 Metal-Organic Framework

Xiao-Min Li,[a] Yameng Wang,[b] Yongbiao Mu,[b] Junkuo Gao,[a] and Lin Zeng*[b,c]*

[a]Dr. Xiao-Min Li, Prof. Junkuo Gao
School of Materials Science and Engineering, Institute of Functional Porous Materials, Zhejiang Sci-Tech University, Hangzhou 310018, China.
E-mail: jkgao@zstu.edu.cn

[b]Yameng Wang, Yongbiao Mu, Prof. Lin Zeng
Department of Mechanical and Energy Engineering, Southern University of Science and Technology, Shenzhen 518055, China.
E-mail: zengl3@sustech.edu.cn

[c]Prof. Lin Zeng
SUSTech Energy Institute for Carbon Neutrality, Southern University of Science and Technology, Shenzhen 518055, China.

Table of Contents

Figure S1-S3 | Scanning Electron Microscopy…….6

Figure S4 | Transmission electron microscopy.....7

Figure S5 | N_2 Adsorption Measurements.....7

Figure S6-S8 | X-ray photoelectron spectroscopy.....8

Table S1 | Elemental analysis.....9

Figure S9-S10 | ^1H SSNMR spectra.....9

Figure S12 | TGA analysis.....11

Figure S13-S15 | Alternating Current Impedance Spectroscopy.....11

Figure S16-S18 | Log-scaled proton conductivities.....13

Figure S19-S21 | Alternating Current Impedance Spectroscopy.....15

Table S2 | Comparisons of σ of samples under hydrous conditions conditions.....16

Figure S22-S23 | Arrhenius plots.....17

Figure S24-S28 | Cycles Measurements.....18

Figure S29-S30 | Time-dependent proton conductivities.....21

Figure S31 | Powder X-ray Diffraction.....22

Reference……..……..22

1. Materials and methods

1.1 Materials preparation

Chemicals: All reagents used in this study were analytical grade and without further purification. All solutions used in this study were prepared with deionized (DI) water (resistivity ≥18.2 MΩ, Millipore Milli-Q). Zirconyl chloride octahydrate ($ZrOCl_2•8H_2O$), benzenetricarboxylic acid (H_3BTC), 1H-imidazole-4-carboxylic acid, 4,5-imidazoledicarboxylic acid were purchased from Aladdin. Ethanol absolute (CH_3CH_2OH), formic acid (HCOOH), N, N-dimethylformamide (DMF) and acetone were purchased from Sinopharm Chemical Reagent Co. Ltd.

Synthesis of MOF-808: MOF-808 was prepared with some modifications according to the method described in the previous literature.[1] $ZrOCl_2•8H_2O$ (0.97 g) and H_3BTC (0.21 g) were dissolved in the DMF/formic acid (30 mL/30 mL). Subsequently, the solution was transferred into a 100 mL autoclave to heat at 100 °C for 24 h. The resulting precipitate was collected by centrifugation and washed with DMF three times and acetone three times, respectively. Finally, the sample was dried at room temperature on a vacuum oven overnight.

Synthesis of MOF-808-IMC: 1H-imidazole-4-carboxylic acid (1 g) was dissolved in the H_2O (30 mL) and then MOF-808 (0.1 g) was added into the solution. Subsequently, the solution was transferred into a 100 mL three-necked flask and the mixture was heated at 90 °C under stirring for 48 hours. The resulting precipitate was collected by centrifugation and washed with H_2O and CH_3CH_2OH. After drying at 80 °C on vacuum overnight, the final material was obtained.

Synthesis of MOF-808-IMDC: 4,5-imidazoledicarboxylic acid (1 g) was dissolved in the DMF (100 mL) and then MOF-808 (0.1 g) was added into the solution. Subsequently, the solution was transferred into a 250 mL three-necked flask and the mixture was heated at 160 °C to reflux for 48 hours. The resulting precipitate was collected by centrifugation and washed with DMF and CH_3CH_2OH. After drying at 80 °C on vacuum overnight, the final material was obtained.

1.2 Characterization methods

The powder X-Ray diffraction (PXRD) patterns were recorded on a Bruker Advance D8 (40 kV, 25 mA) diffractometer equipped with Cu radiation over the 2θ range of 5-50° using a scan speed of 0.1 s/step. Thermogravimetric analyse (TGA) was performed by Diamond TG/DTA/DSC of American Perkin-Elmer Company. N_2 adsorption-desorption isotherms were measured at 77 K on an ASAP 2020 HD88. The samples were activated under N_2 stream at 120 °C for 12 h. Morphology analysis of the composite materials was examined by a scanning electron microscope (SEM, TESCAN MIRA3) at an acceleration voltage of 10 kV. Energy-dispersive X-ray spectroscopy (EDS) was also performed with TESCAN MIRA3. Transmission electron microscopy (TEM) images and elemental mapping were recorded on a Tecnai instrument with an acceleration voltage of 300 kV. The Fourier-transform infrared (FTIR) spectra were measured by a PerkinElmer instrument with a scanning range of 4000-400 cm^{-1}. The X-ray photoelectron spectroscopy measurements were conducted by a ESCALAB Xi+ instrument of Thermo Fisher Scientific company. H_2O adsorption-desorption isotherms were measured at 298K on a Quantachrome Instruments Autosorb AS-6B. The samples were activated under N_2 stream at 120 °C for 12 hours. The SSNMR spectra were performed by a Bruker AVANCE III 600 soectrometer. Elemental analysis was performed with Flash 2000 from Thermo Fisher.

2. Proton conductivity measurements

Firstly, the powder samples were put into a self-made mold with a radius of 0.2 cm for compression to obtain circular pellets and their thicknesses were determined by a vernier caliper. Secondly, the pellets were coated with silver glue on top and bottom sides and dried naturally in the air. Thirdly, the pellets were fixed on the sample holders with gold wires. The proton conductivities of pellets were measured using a quasi-four-probe method with an impedance/gain-phase analyzer (Solartron S1 1260) ranging the frequency from 1 Hz to 1 MHz with an input voltage of 100 mV. The measurements were executed at 30 °C under different relative humidities (40% to 98% RH) and under 98% RH at different temperatures (30 to 70°C), respectively. Subsequently, the values of proton conductivities were calculated using the following equation

$$\sigma = \frac{l}{SR}$$

where σ, l, S and R mean the conductivity (S cm^{-1}), the thickness (cm) of the pellet, the cross-sectional area (cm^2) of the pellet and the bulk resistance (Ω), respectively. The activation energy (Ea) was calculated from the following equation

$$ln\sigma_T = ln\sigma_0 - \frac{E_a}{KT}$$

where σ, K and T mean the conductivity (S cm^{-1}), the Boltzmann constant (eV / K) and the temperature (K), respectively. ZView software was used to get bulk resistance by fitting the semicircle of Nyquist plots and the values of conductivity and activated energy were obtained by calculation following the above equations.

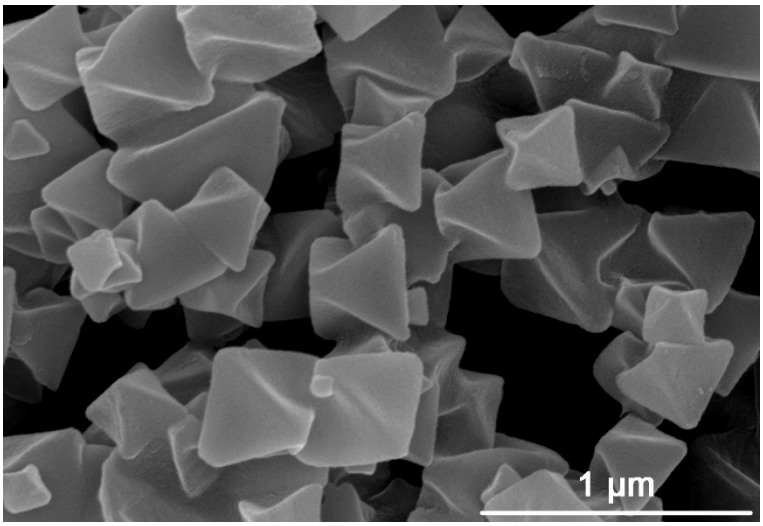

Figure S1. A typical SEM image of MOF-808.

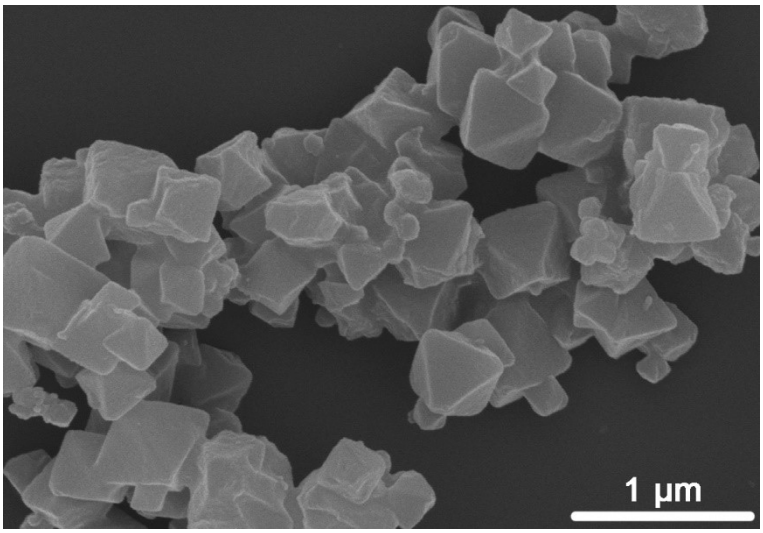

Figure S2. A typical SEM image of **MOF-808-IMC**.

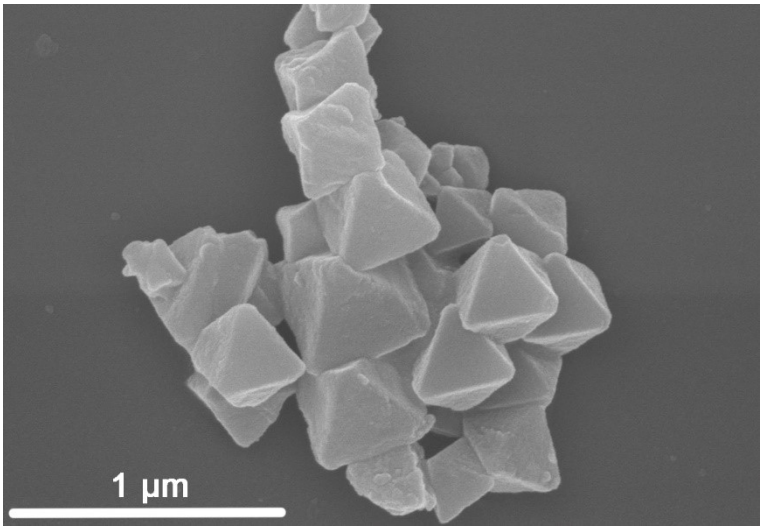

Figure S3. A typical SEM image of **MOF-808-IMDC**.

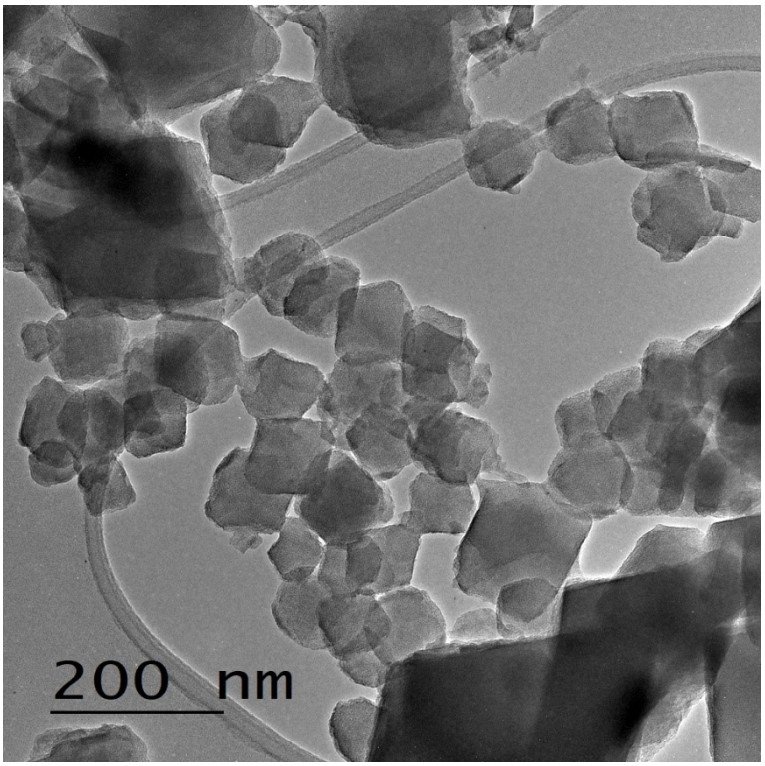

Figure S4. A typical TEM image of MOF-808.

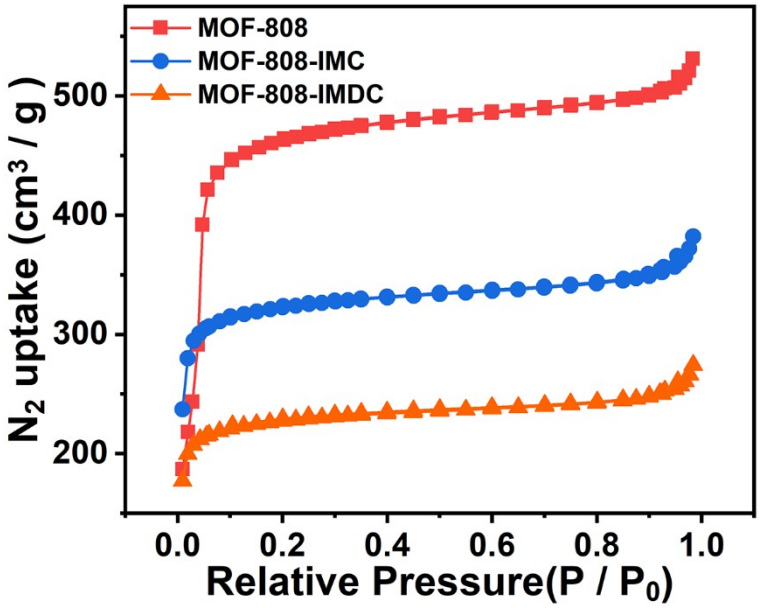

Figure S5. N_2 adsorption-desorption isotherms of MOF-808 (red), **MOF-808-IMC** (blue) and **MOF-808-IMDC** (orange) measured at 77 K.

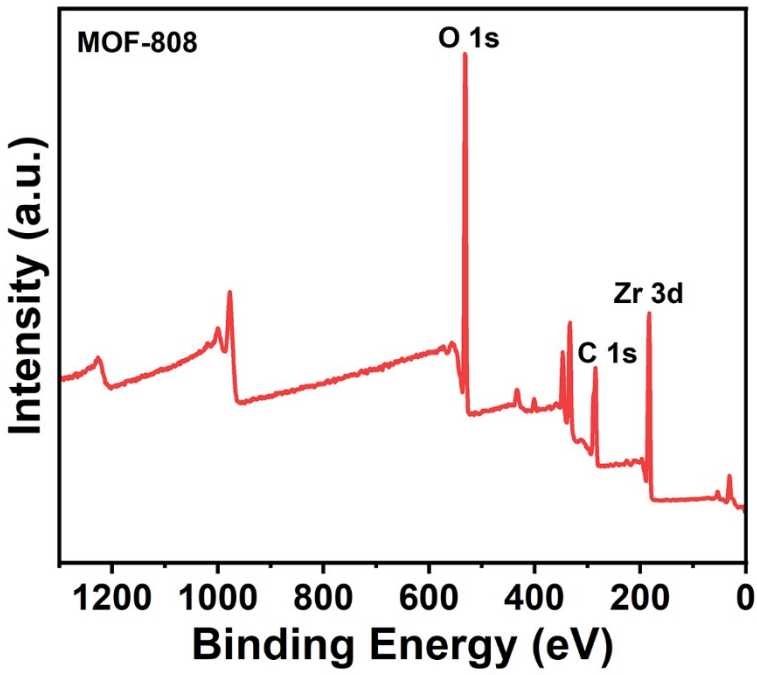

Figure S6. XPS spectrum of MOF-808.

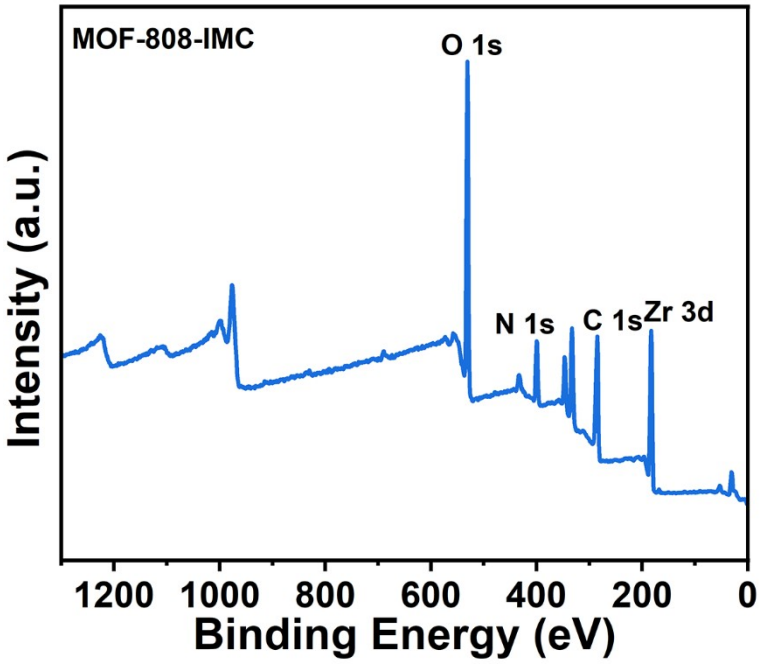

Figure S7. XPS spectrum of **MOF-808-IMC**.

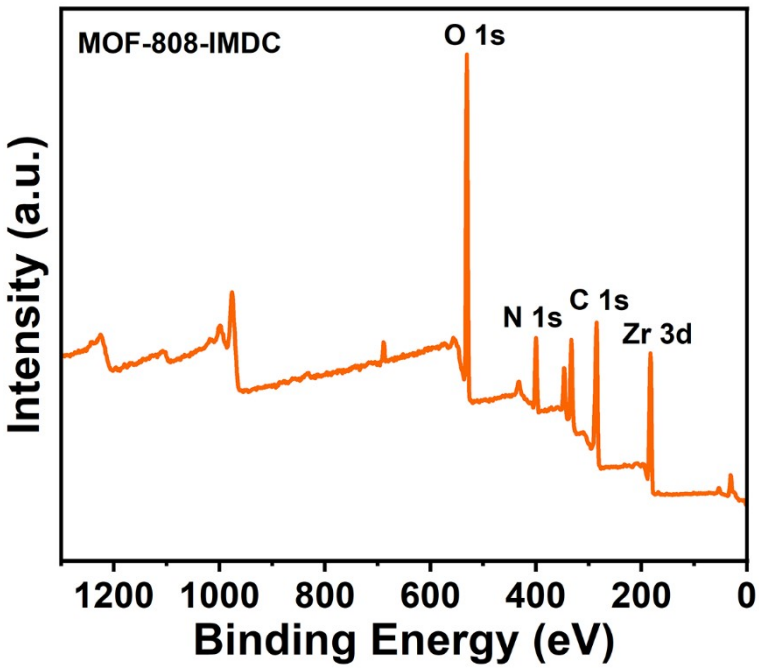

Figure S8. XPS spectrum of **MOF-808-IMDC**.

Table S1. Mass percents of materials with elemental analysis measurements.

Material	C (wt%)	H (wt%)	N (wt%)
MOF-808	20.03	2.15	0
MOF-808-IMC	27.86	2.13	10.04
MOF-808-IMDC	28.21	1.92	8.49

It is calculated that there are about 6 IMC and 5 IMDC connected to a MOF-808 unit, respectively.

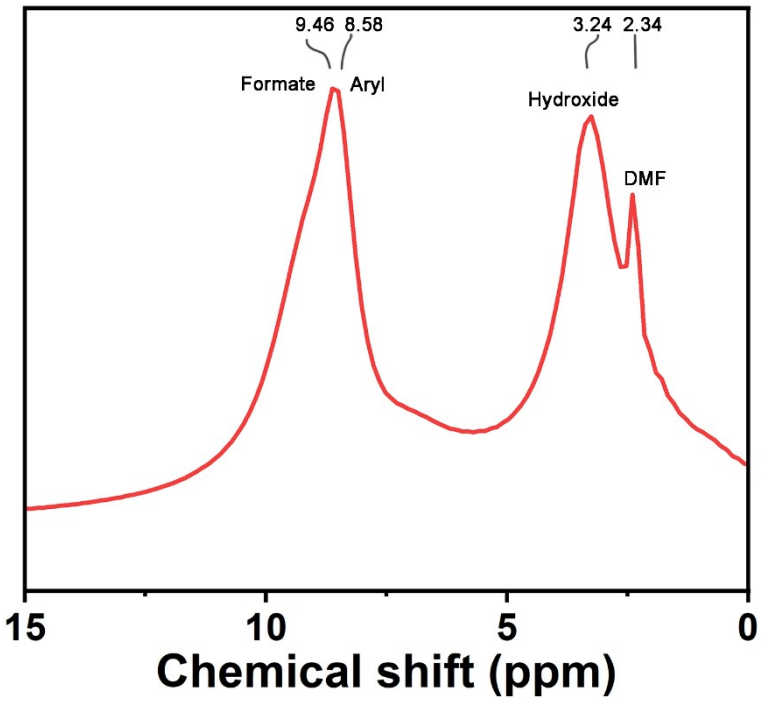

Figure S9. ^{1}H SSNMR spectrum of MOF-808.

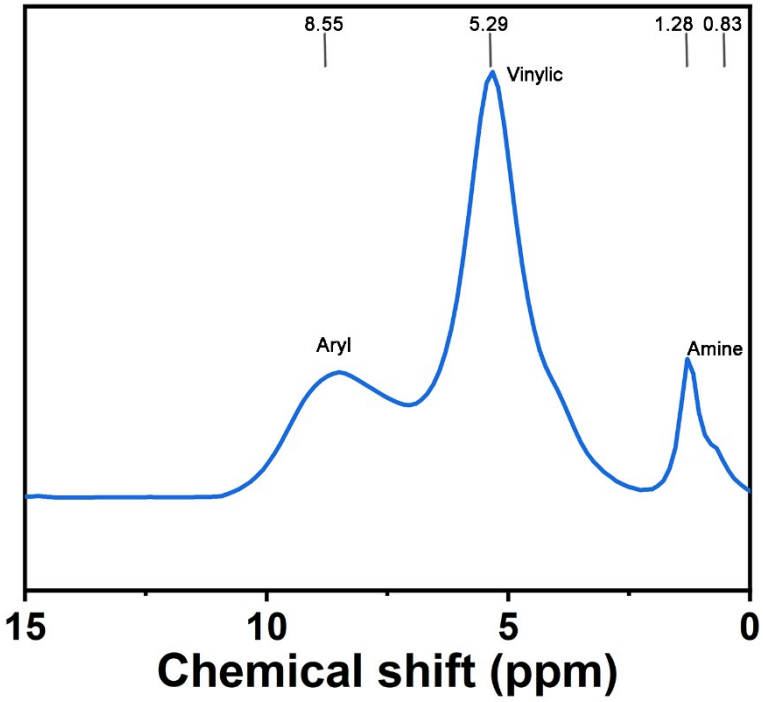

Figure S10. ^{1}H SSNMR spectrum of **MOF-808-IMC**.

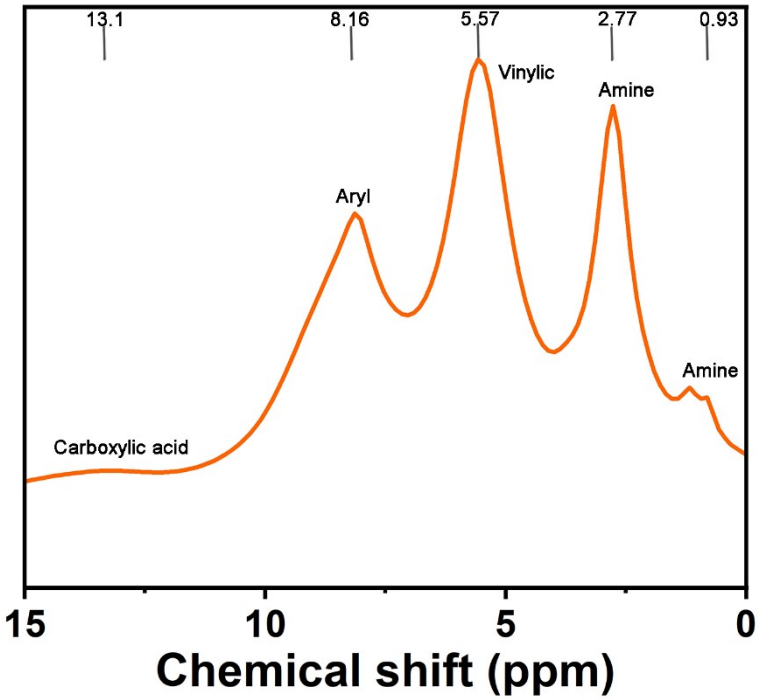

Figure S11. ^{1}H SSNMR spectrum of **MOF-808-IMDC**.

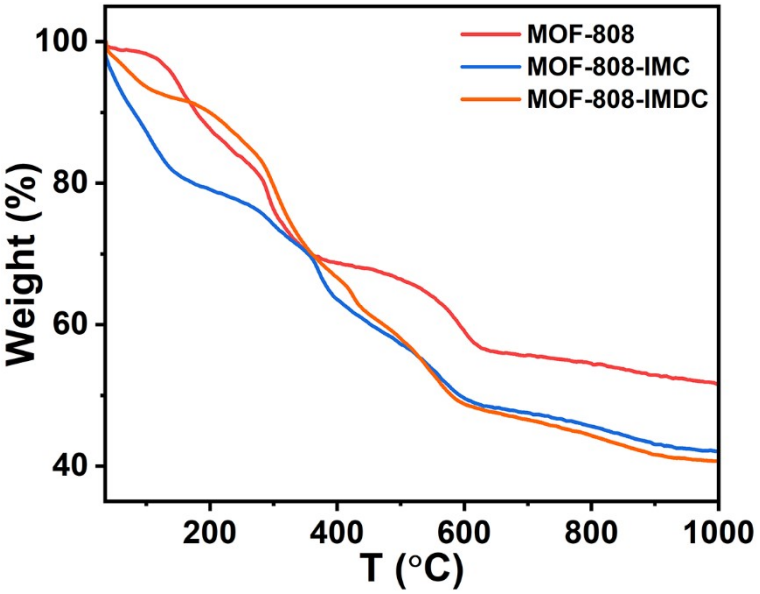

Figure S12. TGA curves of MOF-808 (red), **MOF-808-IMC** (blue) and **MOF-808-IMDC** (orange).

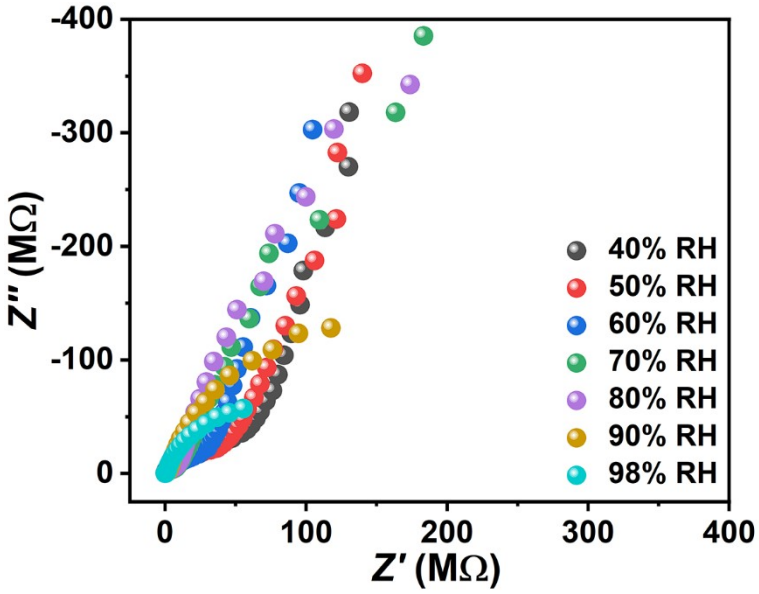

Figure S13. Nyquist plots of MOF-808 at 30 ˚C and different humidities variation from 40% to 98% RH.

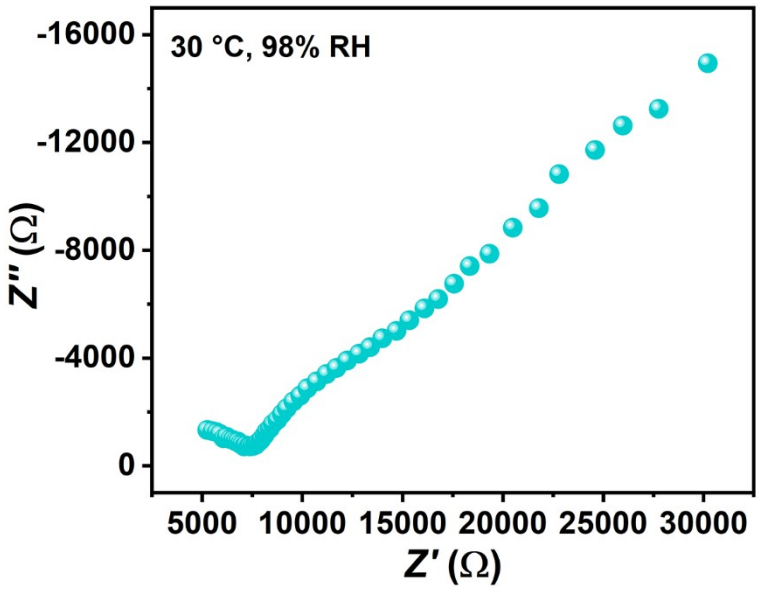

Figure S14. Nyquist plots of **MOF-808-IMC** at 30 ˚C and 98% RH.

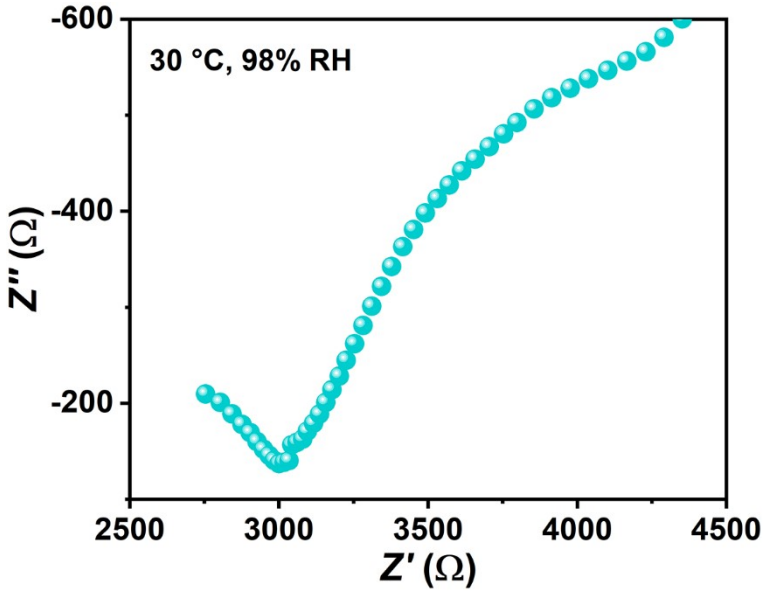

Figure S15. Nyquist plots of **MOF-808-IMDC** at 30 ˚C and 98% RH.

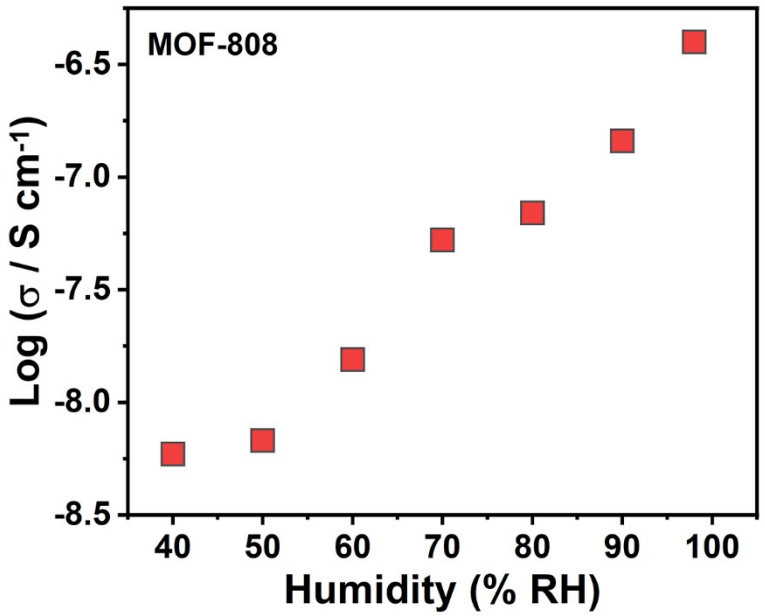

Figure S16. The proton conductivities of MOF-808 at 30 ˚C and different humidities variation from 40% to 98% RH.

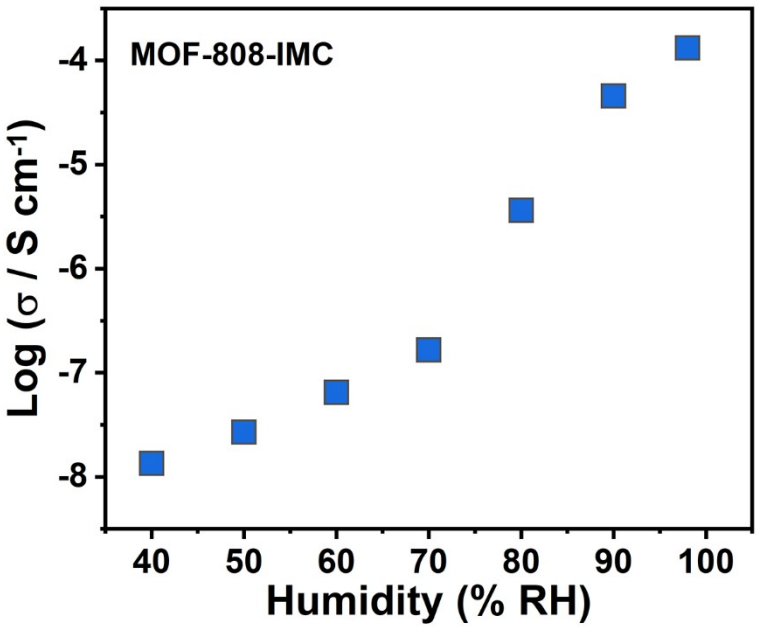

Figure S17. The proton conductivities of **MOF-808-IMC** at 30 ˚C and different humidities variation from 40% to 98% RH.

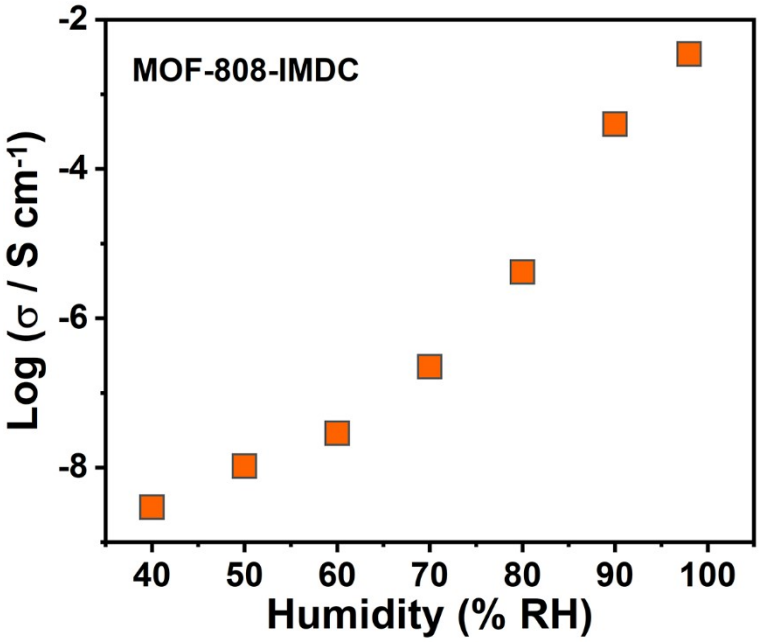

Figure S18. The proton conductivities of **MOF-808-IMDC** at 30 ˚C and different humidities variation from 40% to 98% RH.

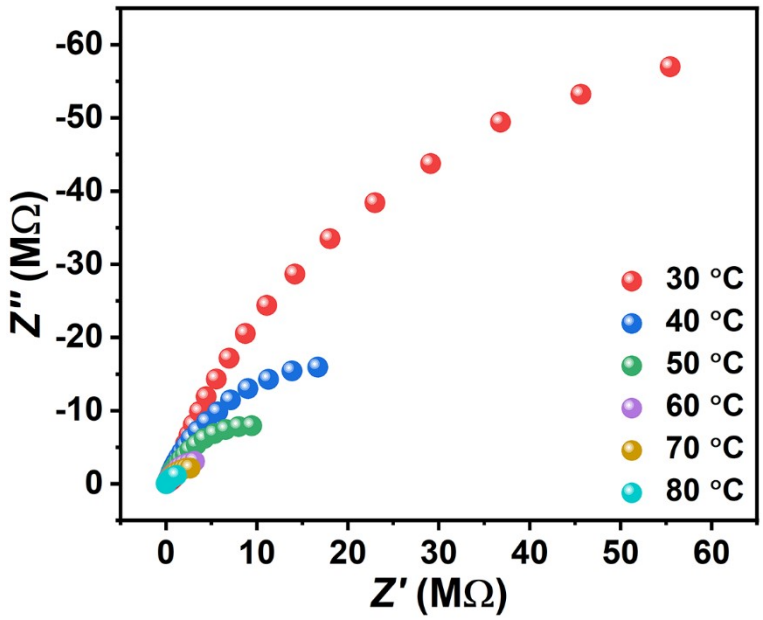

Figure S19. Nyquist plots at 98% RH and different temperatures variation from 30 to 80 ˚C of MOF-808.

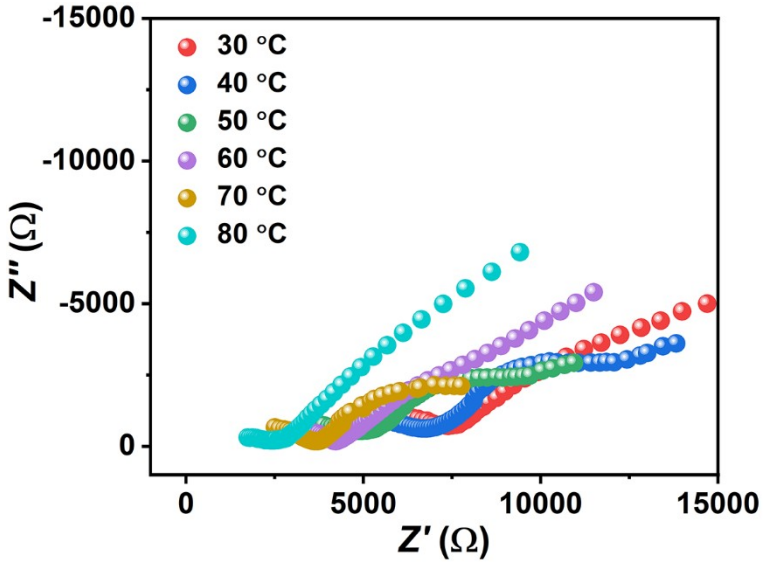

Figure S20. Nyquist plots at 98% RH and different temperatures variation from 30 to 80 ˚C of **MOF-808-IMC**.

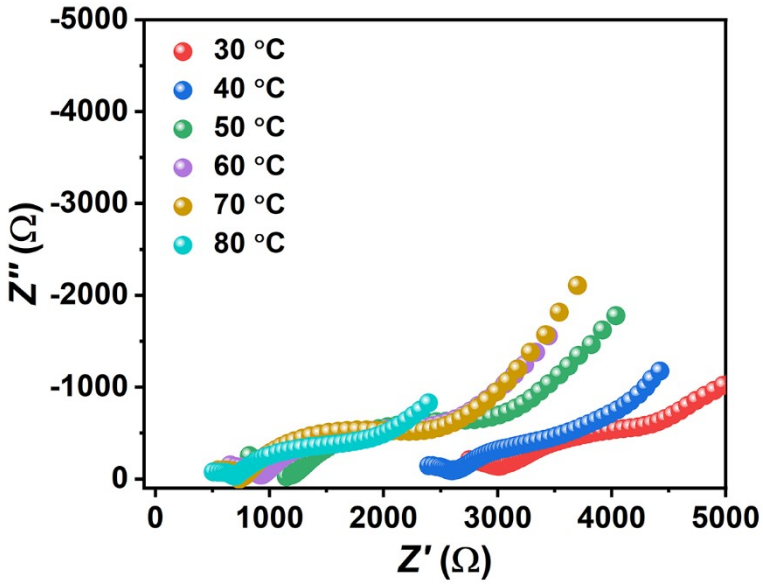

Figure S21. Nyquist plots at 98% RH and different temperatures variation from 30 to 80 ˚C of **MOF-808-IMDC**.

Table S2. Comparison of proton conductivities and activation energies of **MOF-808-IMC** and **MOF-808-IMDC** with Nafion and some other representative MOFs-based intrinsic proton conductors measured under hydrous condition.

Compounds	Conditions	σ (S cm^{-1})	E_a (eV)	Reference
MOF-808-IMC (powder pellet)	80 ˚C, 98% RH	5.04 × 10^{-4}	0.27	This work
MOF-808-IMDC (powder pellet)	80 ˚C, 98% RH	1.11 × 10^{-2}	0.25	This work
Nafion (membrane)	30 ˚C, 98% RH	5 × 10^{-2}	0.22	2
IM-UiO-66-AS (powder pellet)	80 ˚C, 98% RH	1.54 × 10^{-1}	0.20	3
[$(CH_3)_2NH_2$][In(TTFOC)] (powder pellet)	70 ˚C, 98% RH	1.69 × 10^{-2}	0.09	4
MFM-300(Cr)-$SO_4(H_3O)_2$ (powder pellet)	25 ˚C, 99% RH	1.26 × 10^{-2}	0.04	5
EMIM@MIL-101-SO_3H (powder pellet)	70 ˚C, 60%-80% RH	> 1.0 × 10^{-1}	0.22	6
H_2DAB-MgNi$(ox)_3$ (powder pellet)	25 ˚C, 95% RH	5.4 × 10^{-6}	0.17	7

MOF-74(Mg)-Urea (powder pellet)	25 ˚C, 95% RH	2.64×10^{-2}	~0.13	8
MOF-808-4SA-150 (powder pellet)	60 ˚C, 95% RH	7.89×10^{-2}	0.14	9
PMNS1 (powder pellet)	80 ˚C, 100% RH	1.52×10^{-1}	0.15	10

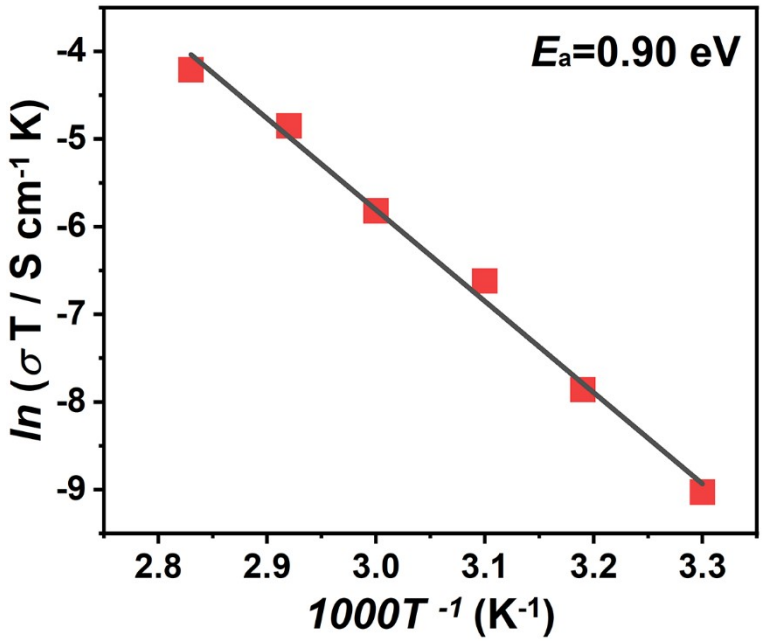

Figure S22. Arrhenius plot of MOF-808 under 98% RH and in the temperature range of 30-80 ˚C.

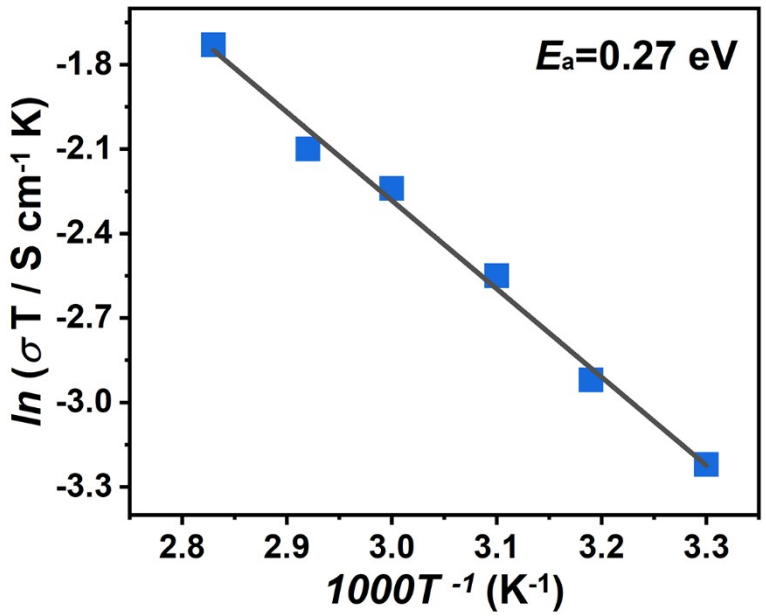

Figure S23. Arrhenius plot of **MOF-808-IMC** under 98% RH and in the temperature range of 30-80 ˚C.

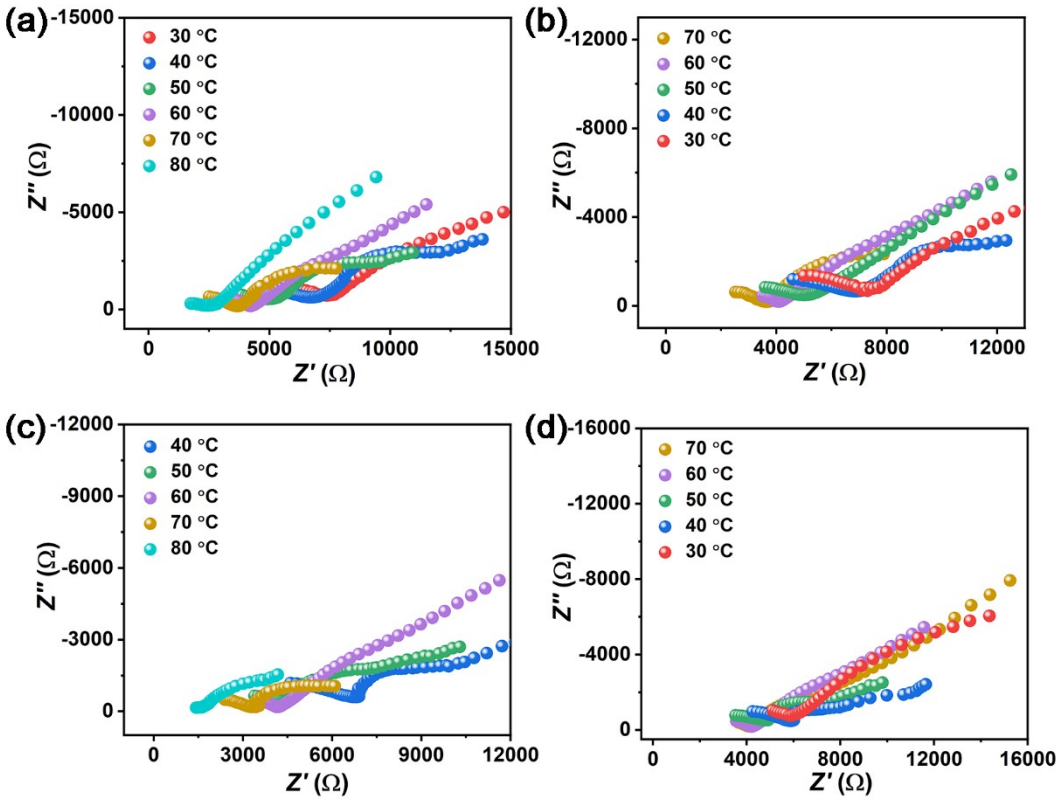

Figure S24. Nyquist plots from AC impedance spectra for the heating-cooling cycles of **MOF-808-IMC** under 98% RH: (a) the first heating cycle (30-80 ˚C); (b) the first cooling cycle (70-30 ˚C); (c) the second heating cycle (40-80 ˚C); (d) the second cooling cycle (70-30 ˚C).

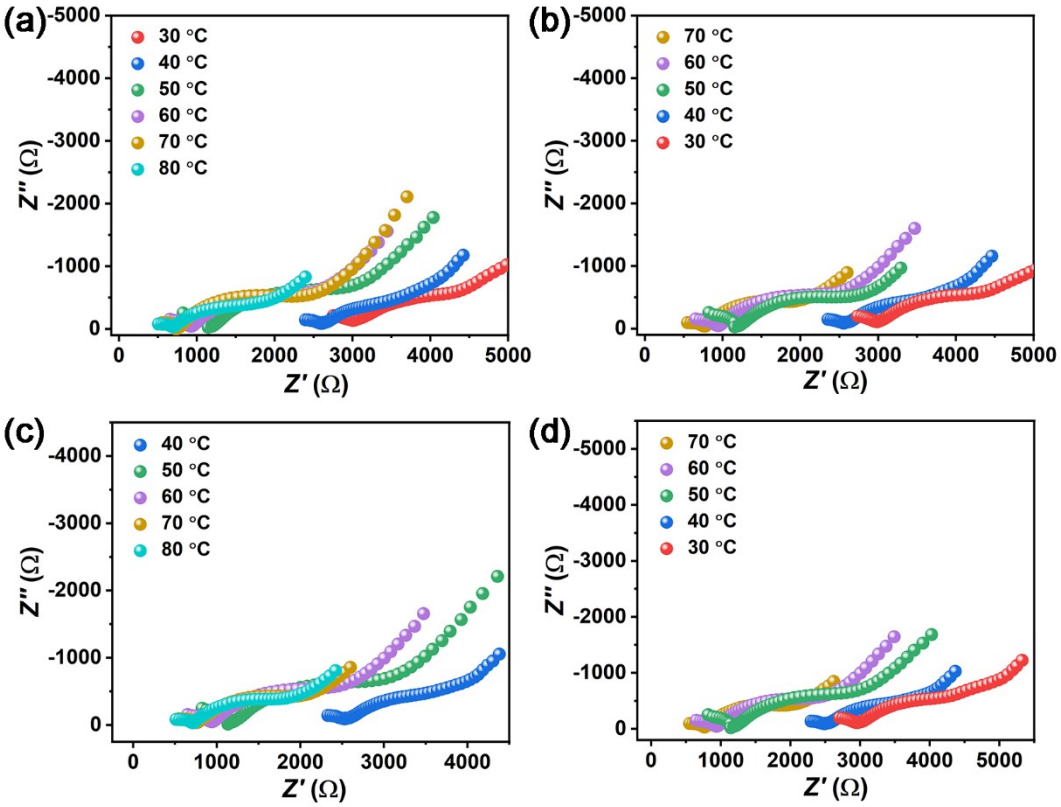

Figure S25. Nyquist plots from AC impedance spectra for the heating-cooling cycles of **MOF-808-IMDC** under 98% RH: (a) the first heating cycle (30-80 ˚C); (b) the first cooling cycle (70-30 ˚C); (c) the second heating cycle (40-80 ˚C); (d) the second cooling cycle (70-30 ˚C).

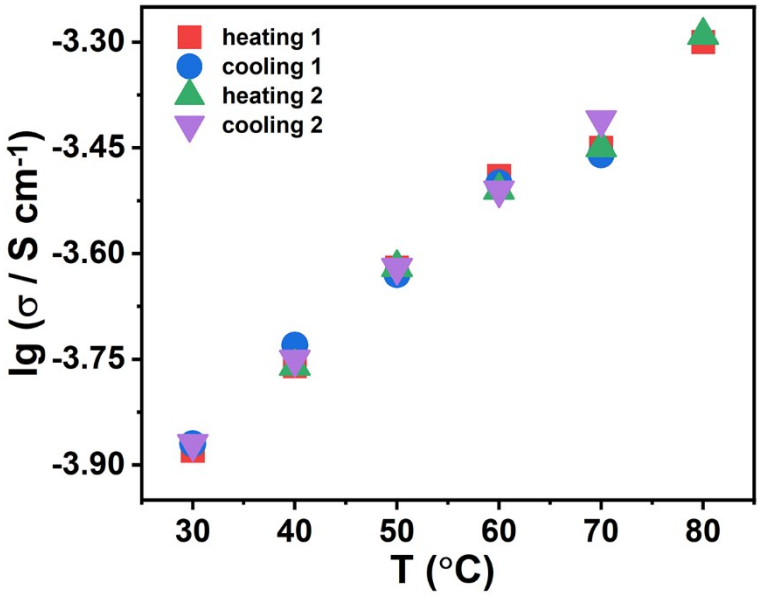

Figure S26. The proton conductivities for the two heating-cooling cycles of **MOF-808-IMC** at 98% RH and within the temperature range of 30-80 ˚C.

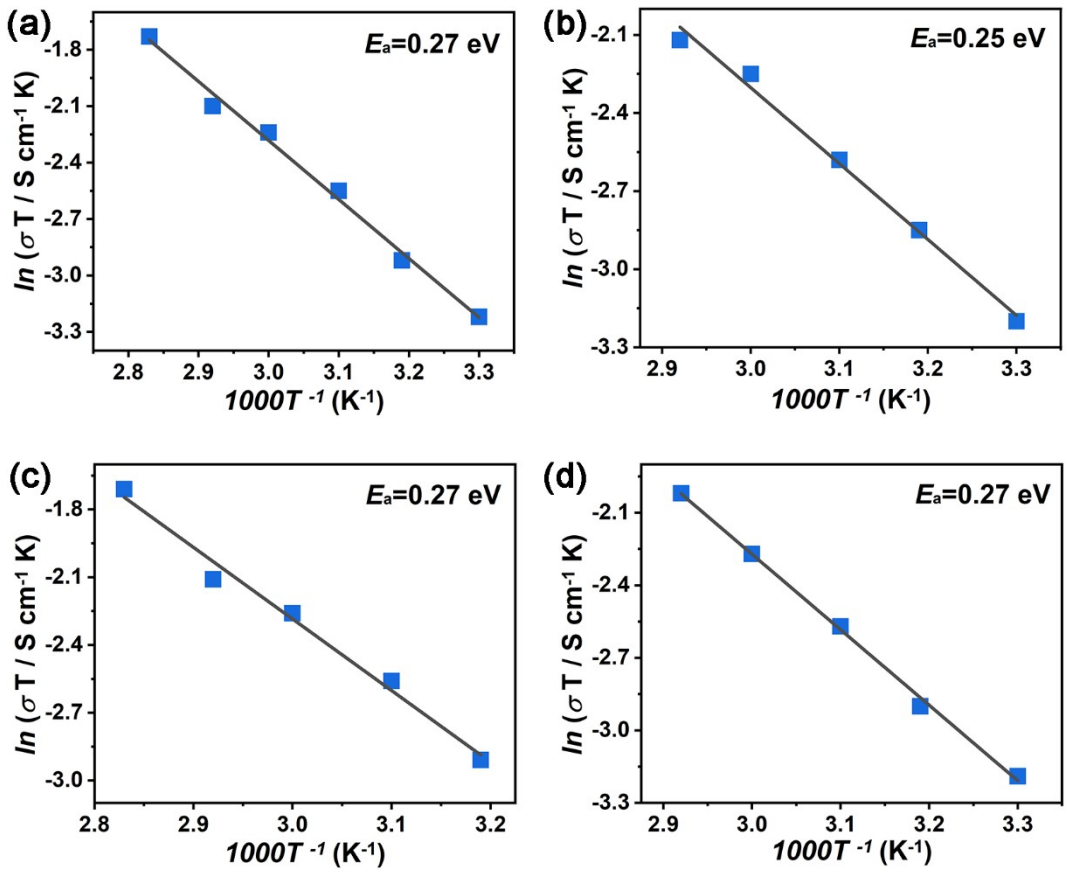

Figure S27. Arrhenius plots of **MOF-808-IMC** for every heating-cooling cycle at the temperature range of 30-80 ˚C and 98% RH: (a) the first heating cycle (30-80 ˚C); (b) the first cooling cycle (70-30 ˚C); (c) the second heating cycle (40-80 ˚C); (d) the second cooling cycle (70-30 ˚C).

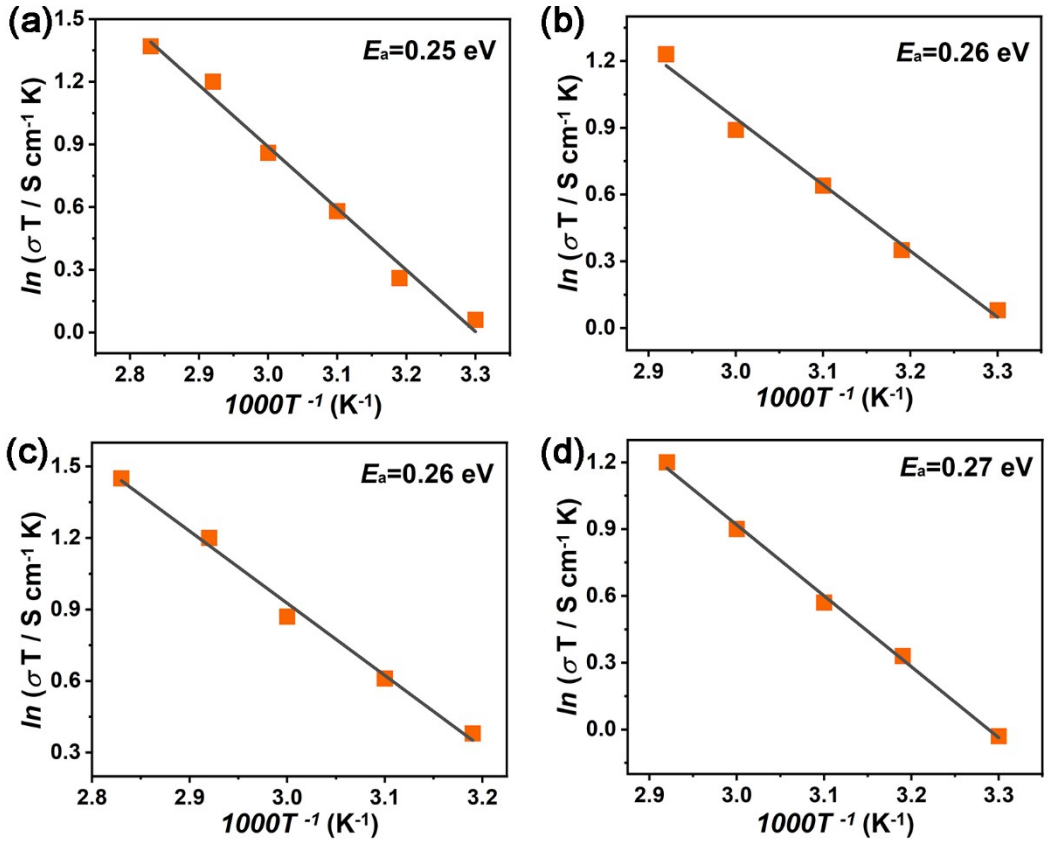

Figure S28. Arrhenius plots of **MOF-808-IMDC** for every heating-cooling cycle at the temperature range of 30-80 ˚C and 98% RH: (a) the first heating cycle (30-80 ˚C); (b) the first cooling cycle (70-30 ˚C); (c) the second heating cycle (40-80 ˚C); (d) the second cooling cycle (70-30 ˚C).

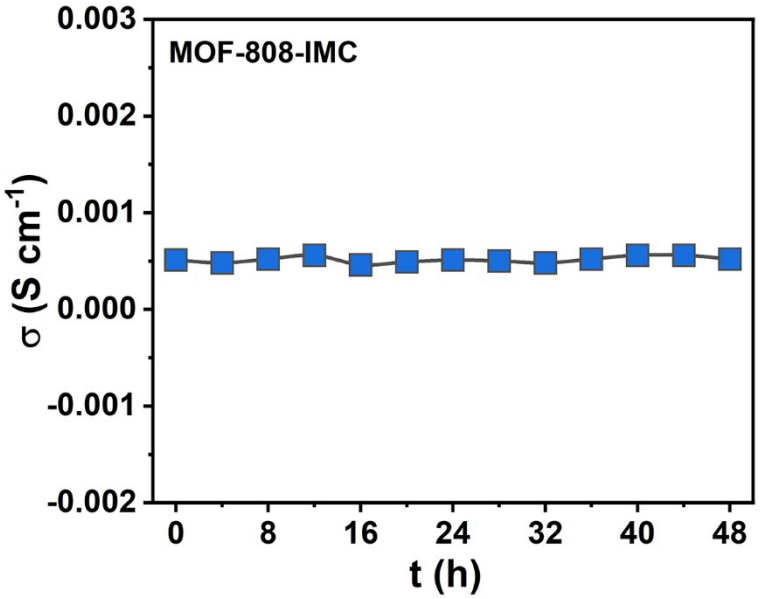

Figure S29. The time-dependent proton conductivities of **MOF-808-IMC** measured at 80 ˚C and 98% RH.

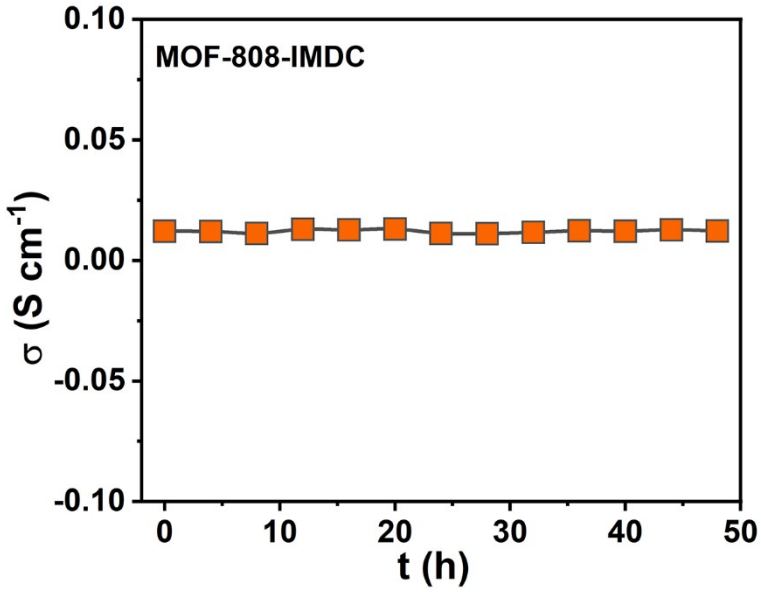

Figure S30. The time-dependent proton conductivities of **MOF-808-IMDC** measured at 80 ˚C and 98% RH.

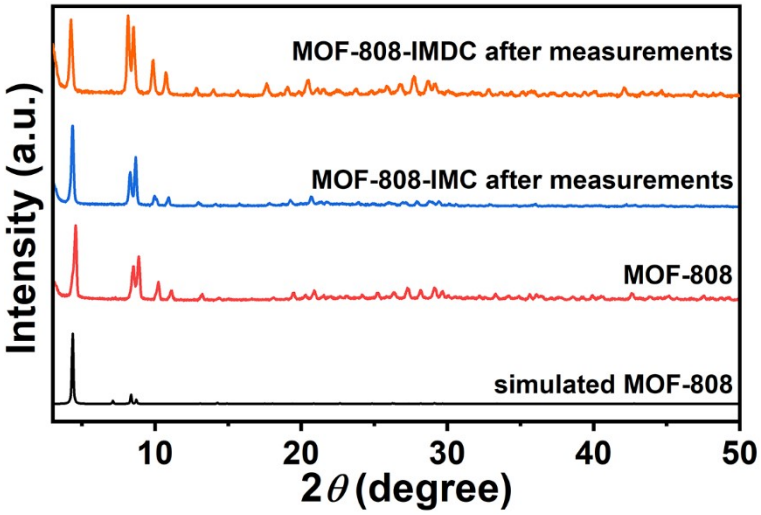

Figure S31. PXRD patterns of simulated MOF-808 (black), as-synthesized MOF-808 (red), **MOF-808-IMC** undergoing proton conduction measurements (blue) and **MOF-808-IMDC** undergoing proton conduction measurements (orange).

References

1. J. Baek, B. Rungtaweevoranit, X. Pei, M. Park, S. C. Fakra, Y.-S. Liu, R. Matheu, S. A. Alshmimri, S. Alshehri, C. A. Trickett, G. A. Somorjai and O. M. Yaghi, *J. Am. Chem. Soc.*, 2018, **140**, 18208-18216.
2. R. C. T. Slade, A. Hardwick and P. G. Dickens, *Solid State Ionics*, 1983, **9-10**, 1093-1098.

3. X.-M. Li, J. Liu, C. Zhao, J.-L. Zhou, L. Zhao, S.-L. Li and Y.-Q. Lan, *J. Mater. Chem. A*, 2019, **7**, 25165-25171.
4. J. Su, W. He, X.-M. Li, L. Sun, H.-Y. Wang, Y.-Q. Lan, M. Ding and J.-L. Zuo, *Matter*, 2020, **2**, 711-722.
5. J. Chen, Q. Mei, Y. Chen, C. Marsh, B. An, X. Han, I. P. Silverwood, M. Li, Y. Cheng, M. He, X. Chen, W. Li, M. Kippax-Jones, D. Crawshaw, M. D. Frogley, S. J. Day, V. García-Sakai, P. Manuel, A. J. Ramirez-Cuesta, S. Yang and M. Schröder, *J. Am. Chem. Soc.*, 2022, **144**, 11969-11974.
6. K. Taksande, E. Gkaniatsou, C. Simonnet-Jégat, C. Livage, G. Maurin, N. Steunou and S. Devautour-Vinot, *Dalton Trans.*, 2021, **50**, 15914-15923.
7. B. Huang and Z. Tan, *Dalton Trans.*, 2022, **51**, 5203-5207.
8. M. K. Sarango-Ramírez, D.-W. Lim, D. I. Kolokolov, A. E. Khudozhitkov, A. G. Stepanov and H. Kitagawa, *J. Am. Chem. Soc.*, 2020, **142**, 6861-6865.
9. A. Sharma, J. Lim, S. Jeong, S. Won, J. Seong, S. Lee, Y. S. Kim, S. B. Baek and M. S. Lah, *Angew. Chem., Int. Ed.*, 2021, **60**, 14334-14338.
10. Z.-H. Li, H. Zeng, G. Zeng, C. Ru, G. Li, W. Yan, Z. Shi and S. Feng, *Angew. Chem., Int. Ed.*, 2021, **60**, 26577-26581.